28th AIAA Applied Aerodynamics Conference
28 June - 1 July 2010, Chicago, Illinois

AIAA 2010-5084

Wing-Wake Interaction and its Proper Orthogonal Decomposition

Zongxian Liang[1], Haibo Dong[2] and Hui Wan[3]
Department of Mechanical & Materials Engineering,
Wright State University, Dayton, OH 45435

Philip Beran[4]
Air Force Research Laboratory
AFRL/RBSD, BLDG 146, 2210 EIGHTH ST
WPAFB, OH 45433

Mingjun Wei[5]
Department of Mechanical and Aerospace Engineering,
New Mexico State University, Las Cruces, NM 88003

Direct numerical simulation (DNS) of tandem wings in pitching and plunging motion is conducted. The POD-Galerkin projection for a fixed, high angle of attack flat plate is performed using two algorithms which differ in the method of pressure processing. It has shown the importance of pressure correction in terms of the reduced prediction error. POD on pitching and plunging wings has shown that most of energy (95%) is contained by the first six modes. However, the first two modes only account for 60% of energy in tandem wings, in contrast to 80% in the case of single wing. It also shows the effectiveness of POD method in a system of two-dimensional flapping tandem wings.

Nomenclature

Φ_i	POD base element of velocity
Ψ_i	POD base element of pressure
$\hat{E}$	Prediction error
U^i	Velocity snapshot
$\overline{U}$	Mean velocity over snapshots
$\mathbf{u}$	Exact velocity field
$\mathbf{u_i}$	Fluctuating velocity field
$\mathbf{u_m}$	Mean velocity field
$\hat{\mathbf{u}}$	Velocity field predicted by Galerkin projection
$\bar{p}$	Mean pressure over snapshots

[1] Ph.D Student, AIAA student member liang.5@wright.edu.
[2] Assistant Professor, AIAA senior member, haibo.dong@wright.edu.
[3] Research Scientist, AIAA member, hui.wan@wright.edu
[4] Principle Aerospace Research Engineer, AIAA associate fellow, Philip.Beran@wpafb.af.mil.
[5] Assistant Professor, AIAA senior member, mjwei@nmsu.edu.

Introduction

Understanding the physics of the vortex dominant flow[1-3] can help the design of micro-air vehicles (MAVs), and reduce the dependence on a trial-and-error approach. The investigation on the tandem wings is motivated by the design of quad-wing MAVs that mimic dragonfly or damselfly flight due to their superior performance in maneuver and endurance[4-7]. The effect of complex wake structures produced by the tandem wings has been studied experimentally[8] and numerically[9-12]. These researches provide great insight into the flow physics such as wing-wake interaction, vortex formation and vortex shedding, and assist the development of more comprehensive aerodynamic models. However, these methodologies are very expensive and not suitable for the purposes of design and control [13, 14]. It is essential to have reduced-order models (ROM) which can describe unsteady physical features in acceptable accuracy and cost. The low order ODE models obtained from Galerkin projection for unsteady forces are ideal for control and design because they fit naturally into existing flight dynamics models. Among various ROM methods, proper orthogonal decomposition (POD) is most commonly used in fluid mechanics, e.g., the wake analysis of flow past single cylinder[15, 16], two cylinders[17] and rod-airfoil[18].

In this paper, POD-Galerkin projection for a fixed, high angle of attack flat plate is first conducted using two algorithms which differ in pressure processing, through which the importance of pressure correction in POD has presented. Single and tandem wings in pitching and plunging motion are studied next. The first six modes capture approximately 95% of kinetic energy. It has shown the effectiveness of POD method in a system of two-dimensional flapping wings.

Direct Numerical Simulation

The non-dimensional incompressible Navier-Stokes equations, as written in Eq. (1),

$$\frac{\partial u_i}{\partial x_i} = 0; \quad \frac{\partial u_i}{\partial t} + \frac{\partial u_i u_j}{\partial x_j} = -\frac{\partial p}{\partial x_i} + \frac{1}{\mathrm{Re}} \frac{\partial^2 u_i}{\partial x_j \partial x_j} \tag{1}$$

are discretized on a Cartesian mesh using second-order central difference scheme in space. A second-order accurate fractional-step method for time advancement is employed. Its key feature is that simulations with complex boundaries can be carried out on stationary non-body conformal Cartesian grids, eliminating the need for complicated re-meshing algorithms that are usually employed with conventional Lagrangian body-conformal methods. The boundary conditions on the immersed body are imposed through a "ghost-cell" procedure [19]. The pressure Poisson equation is solved using the geometric multi-grid method integrating with the immersed-boundary methodology.

Proper Orthogonal Decomposition (POD)

Proper Orthogonal Decomposition is a method used to represent large data fields with a relatively small number of elements. POD creates a set of basis function which spans the original data set by capturing the characteristic components. The system can be represented by the first few dominant modes.

Let $\left\{U^i(x):1\le i\le N, x\in\Omega\right\}$ be a set of N snapshots on domain **Ω**. The mean velocity of the snapshots is given by $\bar{U}=\frac{1}{N}\sum_{i=1}^{N}U^i(x)$. Thus the new snapshots of the fluctuating velocity are $u_i=U^i-\bar{U}$, $i=1,\ldots,N$. It has been shown in previous work[16, 19] that an eigenvalue problem of a coefficient matrix *A* can be constructed using snapshots of $\mathbf{u_i}$ as

$$AV=\lambda V \tag{2}$$

where the entry of matrix *A* is $a_{ij}=\int_\Omega u_i(x)u_j(x)dx$. After solving the eigenvalue problem, the eigenvalue λ_i and corresponding eigenvector V_i are usually reorganized in descending order. Each POD basis elements, Φ_i, is given by $\Phi_i=\sum_{j=1}^{N}a_j^i u_j$ where a_j^i is the *j*-th element of the *i*-th eigenvector, V_i. Based on Φ_i, any snapshot can then be reconstructed using a linear combination of the POD basis elements $U^n=\bar{U}+\sum_{i=1}^{N}\alpha_i^n\Phi_k$ where $\alpha_i^n=\Phi_i\cdot u_n$

Galerkin Projection

The basis function produced by POD is used to generate a predictive model via a Galerkin projection of the incompressible Navier-Stokes equations, Eq. (1). For the velocity field, the Galerking approximation is

$$\left(\Phi_i,\frac{\partial U}{\partial t}+(U\cdot\nabla)U\right)+(\Phi_i,\nabla p)=-\frac{1}{\mathrm{Re}}(\nabla\Phi_i,\nabla U)+\frac{1}{\mathrm{Re}}[\Phi_i\nabla U] \tag{3}$$

in which $(\vec{a},\vec{b})=\int_\Omega\vec{a}\cdot\vec{b}d\Omega$ denotes the inner product of two vectors over domain Ω, and $[\Phi_i\nabla u]=\oint_c\Phi_i\cdot\frac{\partial u}{\partial n}ds$ is the boundary integration over *S*. In Eq. (3), term $(\Phi_i,\nabla p)$ can be further derived as

$$(\Phi_i,\nabla p)=[p\Phi_i] \tag{4}$$

using integration by parts and the divergence free condition. With velocity and pressure conditions properly posed[13, 15], Eq. (4) is approximately zero. This yields the following set of evolution equations for the mode amplitude $\alpha_i(t)$

$$\frac{d\alpha_i^n}{dt}=a_i+\sum_{j=1}^{N}b_{ij}\alpha_i^n+\sum_{j=1}^{N}\sum_{k=1}^{N}c_{ijk}\alpha_j^n\alpha_k^n \tag{5}$$

where

$$\begin{aligned}
a_i&=-(\Phi_i,(\bar{U}\cdot\nabla)\bar{U})-\frac{1}{\mathrm{Re}}(\nabla\Phi_i,\nabla\bar{U})+\frac{1}{\mathrm{Re}}[\Phi_i\nabla\bar{U}]\\
b_{ij}&=-(\Phi_i,(\Phi_j\cdot\nabla)\bar{U})-(\Phi_i,(\bar{U}\cdot\nabla)\Phi_j)-\frac{1}{\mathrm{Re}}(\nabla\Phi_i,\nabla\Phi_j)+\frac{1}{\mathrm{Re}}[\Phi_i\nabla\Phi_j]\\
c_{ijk}&=-(\Phi_i,(\Phi_j\cdot\nabla)\Phi_k)
\end{aligned} \tag{6}$$

In our study, general velocity and pressure boundary conditions are employed, thus term $\left[p\Phi_i\right]$ does not vanish. The effect of pressure gradient is considered by two POD algorithms. In the first algorithm (**A1**), the pressure is decomposed as the sum of mean and fluctuating pressure (Eq. (7), [20]), similar to the expression of POD of velocity field.

$$p^n = \overline{p} + \sum_{i=1}^{N} \beta_i^n \Psi_k \tag{7}$$

In the second algorithm (**A2**), mean pressure is embedded, as expressed in Eq. (8).

$$p^n = \sum_{i=1}^{N} \beta_i^n \Psi_k \tag{8}$$

The decomposition of velocity and pressure into mean and fluctuation are commonly used in turbulence study in which the suitable average of fluctuating velocity and pressure is zero, i.e. $\left\langle \sum_{i=1}^{\infty} \alpha_i^n \Phi_k \right\rangle = \left\langle \sum_{i=1}^{\infty} \beta_i^n \Psi_k \right\rangle = 0$. The POD of fluctuating velocity measures the turbulent kinetic energy while the inner product of fluctuating pressure does not have the straight forward physical meaning. Thus, it is necessary to re-inspect the effectiveness of decomposition in realistic applications, especially for low Reynolds number flow. As will be used later, the prediction error is defined the same way in Graham et al. (1997), in which it is given as a ratio of follows:

$$\hat{E} = \frac{(\mathbf{u} - \hat{\mathbf{u}}, \mathbf{u} - \hat{\mathbf{u}})}{(\mathbf{u} - \mathbf{u}_m, \mathbf{u} - \mathbf{u}_m)} \tag{9}$$

Results

A. Stationary wing at 30° angle of attack

A 2-D stationary membrane airfoil in a flow field with free stream velocity U_∞=1 is shown in Figure 1. The velocity on Γ_1, Γ_3 and Γ_4 is of Dirichlet boundary condition, and on Γ_2 is of Neumann boundary condition. The pressure on all the four boundaries is of homogeneous Neumann boundary condition. Reynolds number is 200. The angle of attack of airfoil is 30°. Snapshots (60 frames per period) are taken after the flow field has reached steady state, at which periodic vortex street in the wake is obtained.

The importance of pressure term (Eq. (4)) in POD is first investigated. The Galerkin projection for algorithms A1 and A2 (as mentioned before) are conducted and the prediction error $\hat{E}$ is compared with result from the case of neglecting the pressure term. The prediction error is plotted against time in figure 2 for the three cases. It can be clearly seen that ignoring the pressure term can bring in salient prediction error over time, which can be substantially reduced by taking care of the pressure term in POD. A1 and A2 work almost equally well in suppressing the prediction error. The projection error[13] is also calculated after reconstructing the original snapshots using 32 modes. The projection error is not shown here, since the maximum error magnitude is at of 10^{-5}.

The eigenvalue spectrum from POD is shown in Figure 3.To achieve an accuracy of 10^{-6}, fourteen and thirteen modes are used in A1 and A2 respectively. Except the first mode, the normalized eigenvalues of A2 follow a very simliar trend as those of A1. Moreover, the eigenvalues from A2 go to zero faster than those from A1. Thus, less modes can be used to

represent the original pressure fields. The first four modes contain nearly over 98% pressure information in the flow field in both A1 and A2. Contours of pressure modes are illustrated in Figure. The mode pattern of mean pressure from A1 (Fig. 4a) is pretty close to the first mode from A2 (Fig. 4b). The position of local extremum of mode 1 from A1(Fig. 4c) are close to that of mode 2 from A2(Fig. 4d). Mode 2 of A1(Fig. 4e) and mode 3 of A2 (Fig. 4f) are analogical to their prior modes.

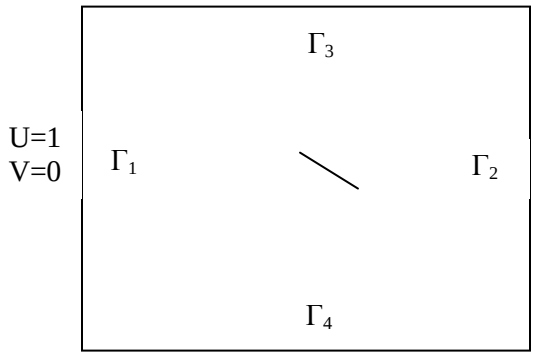

Figure 1 Flow domain of 2-D stationary airfoil

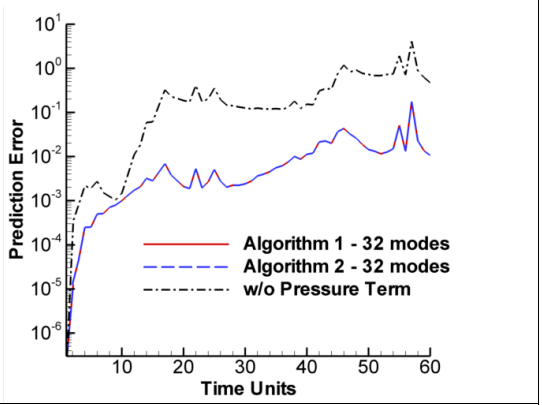

Figure 2 A semi-log graph of prediction error

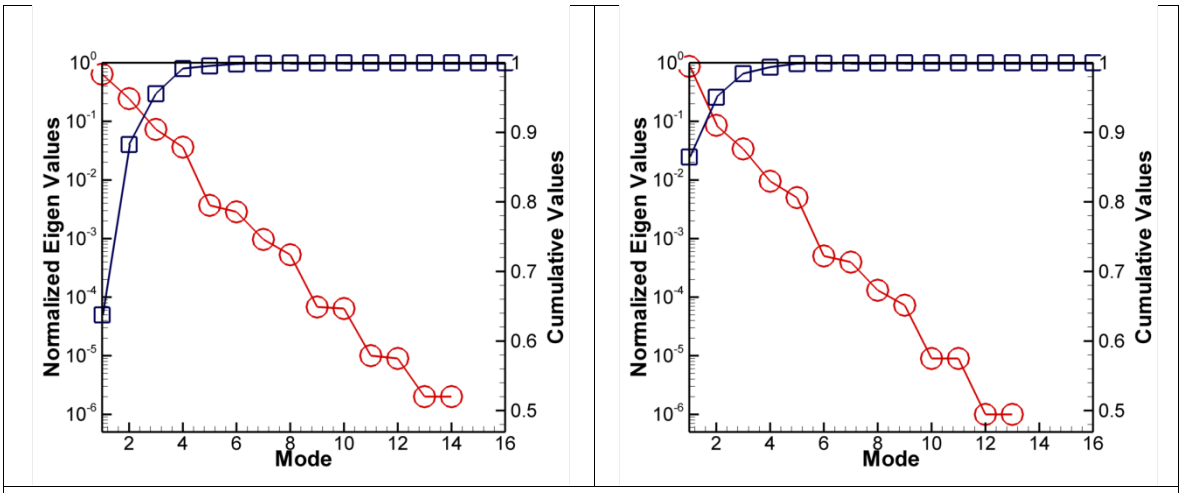

Figure 3. Eigenvalue spectrum of pressure. Left column: Algorithm 1; Right column: Algorithm 2. Curve with circle is for normalized eigen values. Curve with square is for cumulative energy.

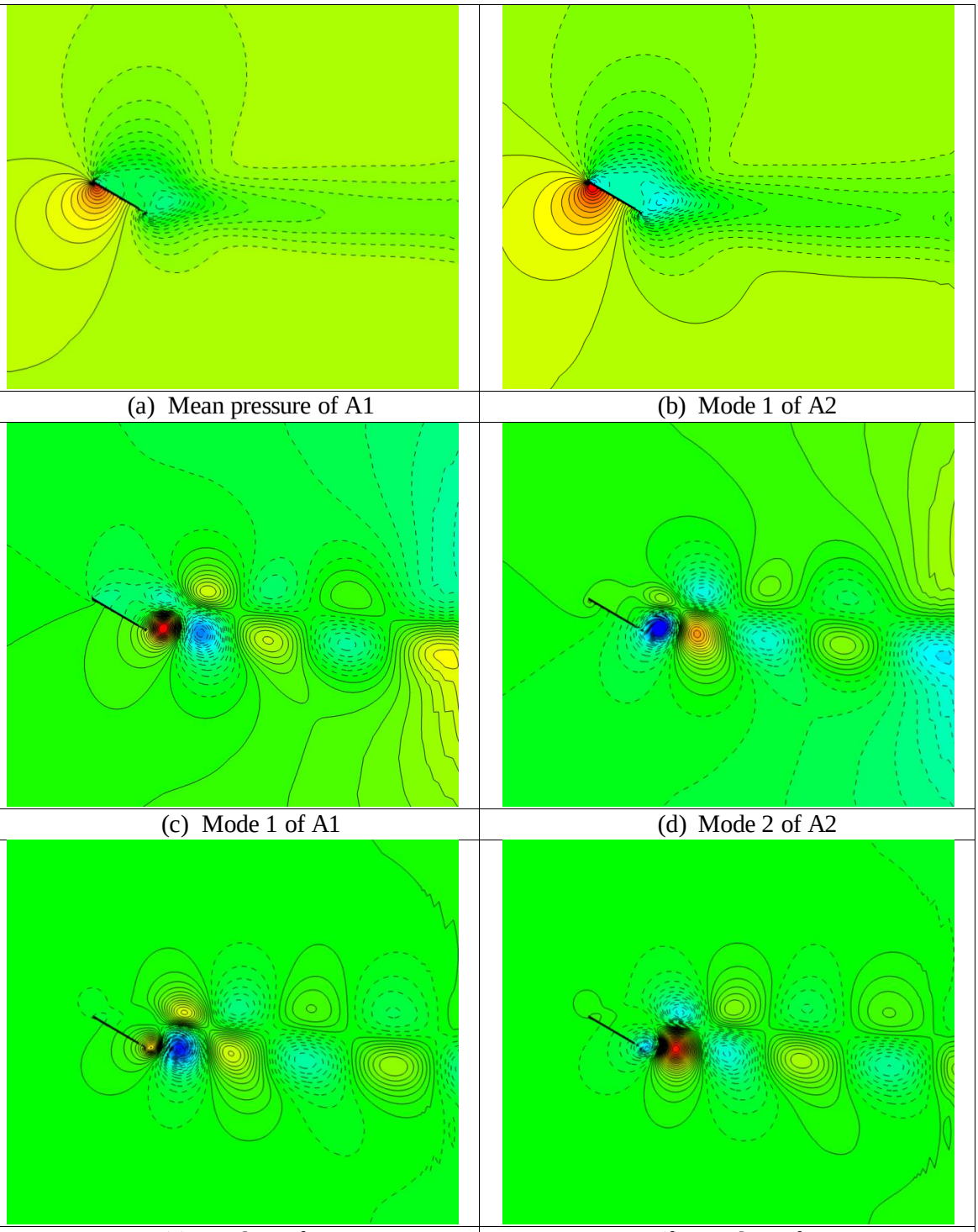

(a) Mean pressure of A1 | (b) Mode 1 of A2

(c) Mode 1 of A1 | (d) Mode 2 of A2

(e) Mode 2 of A1 | (f) Mode 3 of A2

Figure 4. Pressure mode contours. Left column: Algorithm 1; Right column: Algorithm 2. The solid lines indicate a positive contour and the dashed lines indicate a negative contour.

The amplitudes of the first four basis functions present in velocity snapshots are shown in Figure 5. The results from A1 are shown here only. The amplitudes of basis functions from A2

(not plotted) are almost identical to those from A1 due to the effect of pressure term in Eq. (3) is small. The modes from the reduced-order modeling almost exactly match the predicted results from Galerkin projection.

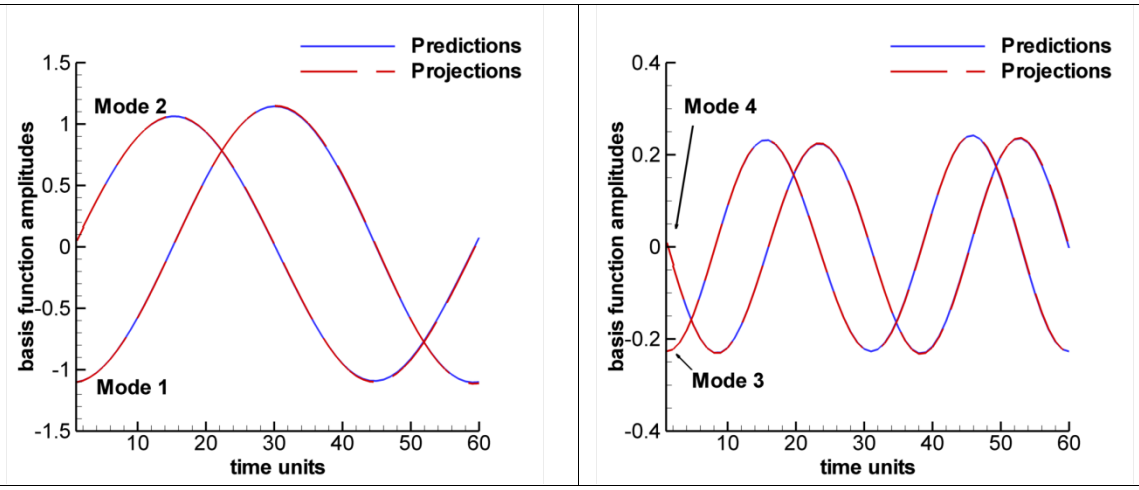

Figure 5. Amplitude for the first four modes
Left: The first and second modes of velocity; right: the third and fourth modes.

B. Single flapping wing

In this section, DNS and POD are conducted on a single wing in pitching and plunging. The kinematics is described by

$$\theta(t) = \theta_{\mathrm{m}} \cos(\omega t + \delta) \tag{10}$$

$$y(t) = A \sin(\omega t + \delta) \tag{11}$$

Reynolds number is 600. The vorticity in the wake is presented in figure 6.

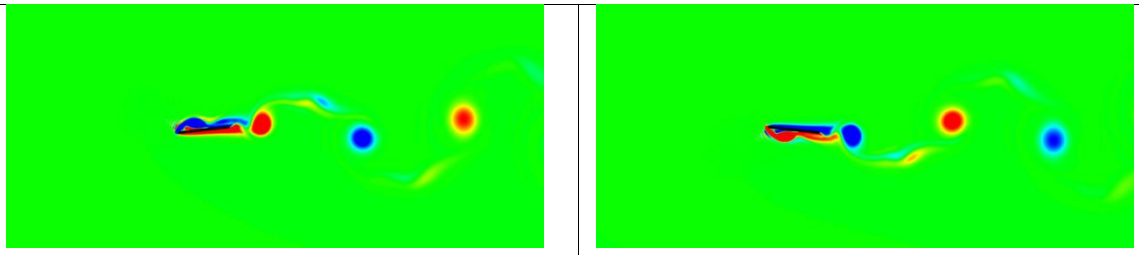

t/T = 0.5 | t/T = 1.0

Figure 6 Vorticity of a single wing in pitching and plunging

POD is conducted over the whole flow domain, with 40 snapshots obtained at regular intervals over one period. The eigenvalue spectrum of a single pitching and plunging wing is shown in figure 7, in which modes are paired by energy levels.

Compared to the flow over a stationary body[15], the distinction in pitching and plunging motions is that the energy level of modes 5 and 6 is very close to that of 3 and 4, and all the four modes are paired together. Same trend happens to modes 7 to 10. Approximately 80% of kinetic energy is taken by the first two modes, and 95% by the first 6 modes.

The velocity contours for the first six modes are shown in figure 7. Note the pairing of similar patterns, shifted spatially, as a result of the convective nature of the flow. Mode 1 and mode 2 come in pairs and have the similar pattern, in both x and y directions, except a phase shift of π approximately.

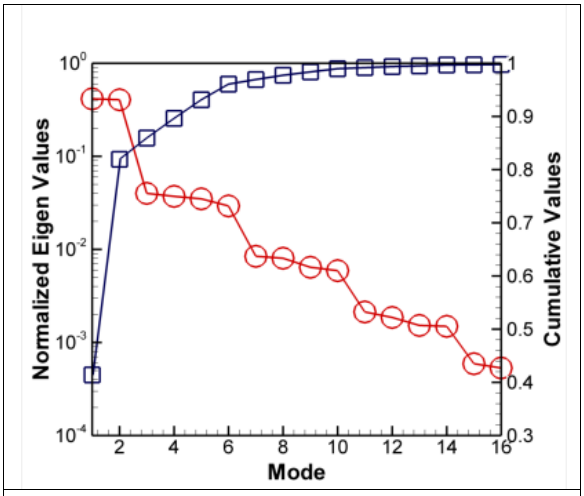

Figure 7 Eigenvalue spectrum of a single wing

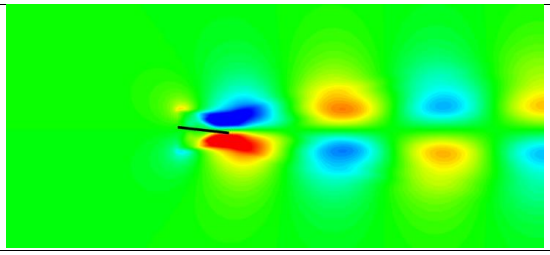

Mode 1 x-direction

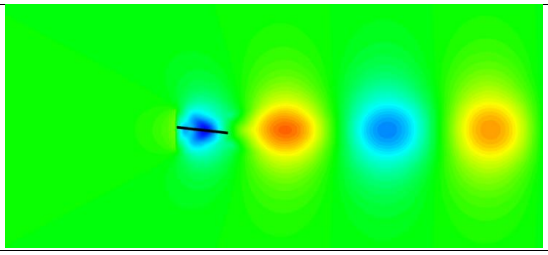

Mode 1 y-direction

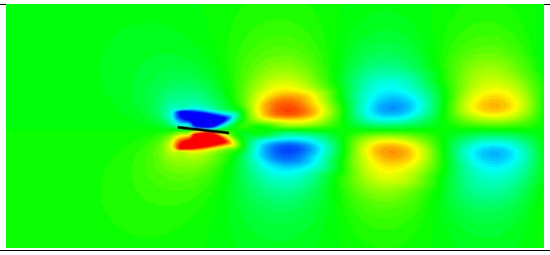

Mode 2 x-direction

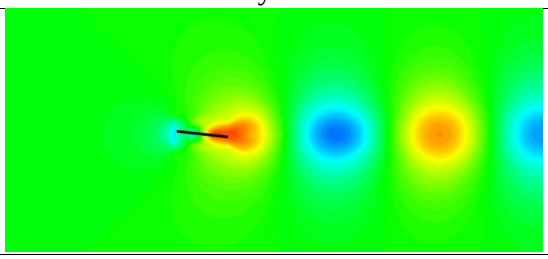

Mode 2 y-direction

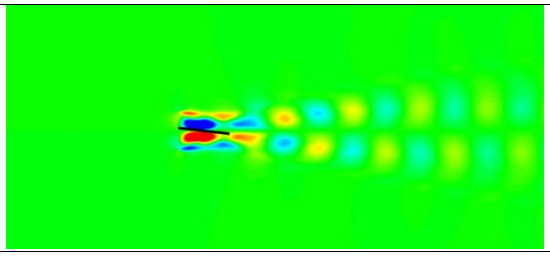

Mode 3 x-direction

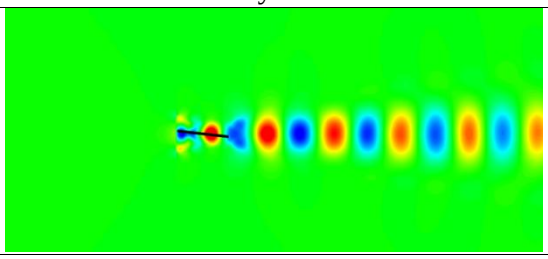

Mode 3 y-direction

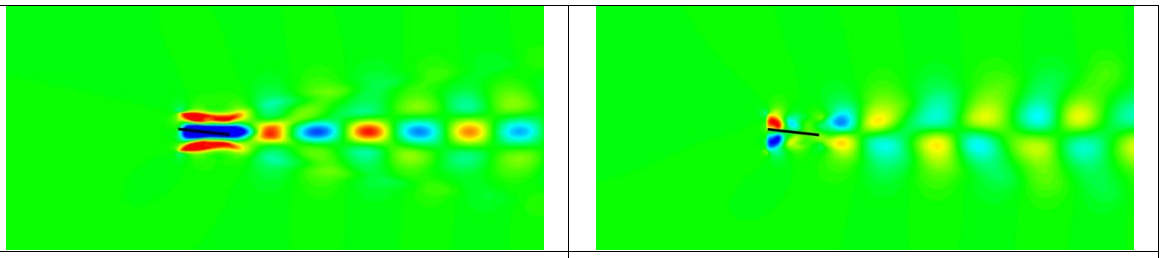

Mode 4 x-direction | Mode 4 y-direction

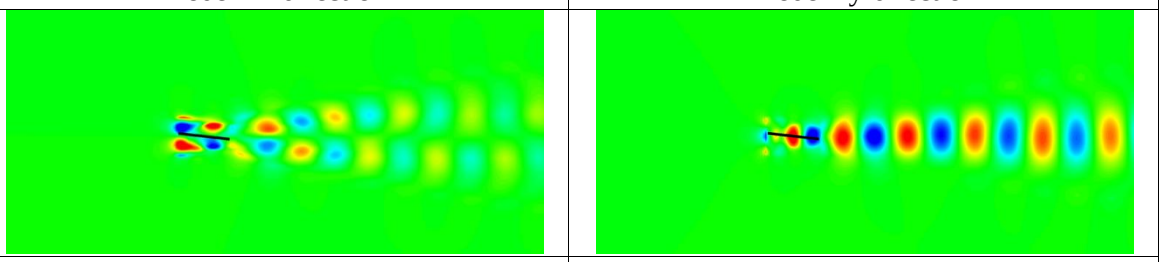

Mode 5 x-direction | Mode 5 y-direction

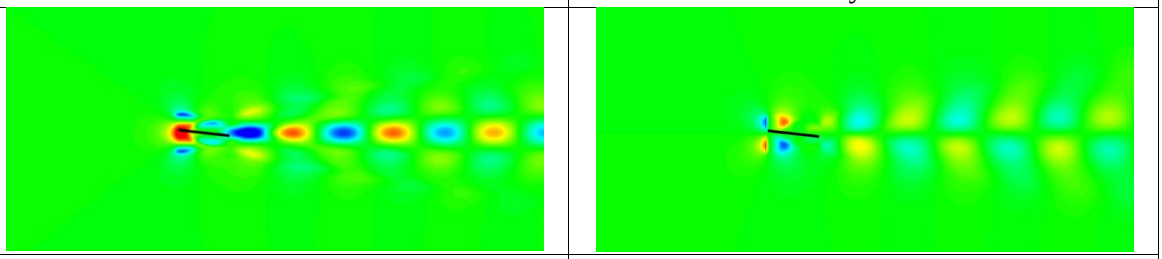

Mode 6 x-direction | Mode 6 y-direction

Figure 8 Velocity POD mode of a single wing in pitching and plunging

C. Two tandem wings with different phase difference

The same kinematics is used for tandem wings as for the single wing in previous section. The phase angle δ is 0 °for the fore wing, and -48 °for the hind wing. More control parameters of the motion are listed in Table 1.

Table 1: Control Parameters

Parameter	Fore wing	Hind wing
θ_m	6.4 °	9.5 °
A/c	0.32	0.56
Δ	0 °	-48 °
Chord ratio (c_f /c_h)	1.0	—
Re=$U_\infty c/\nu$	600	—
St= f 2A/U_∞	—	0.28

The ratio of the stream-wise distance between the central of two wings to the chord of wing is 2. The Reynolds number is 600, based on the free stream velocity and the chord length of hindwing. The fore wing leads the hind wing by 48 ° of phase difference. The parameters of motion and flow field are similar to those described in [21]. The vortex sheet in the wake is shown in figure 9.

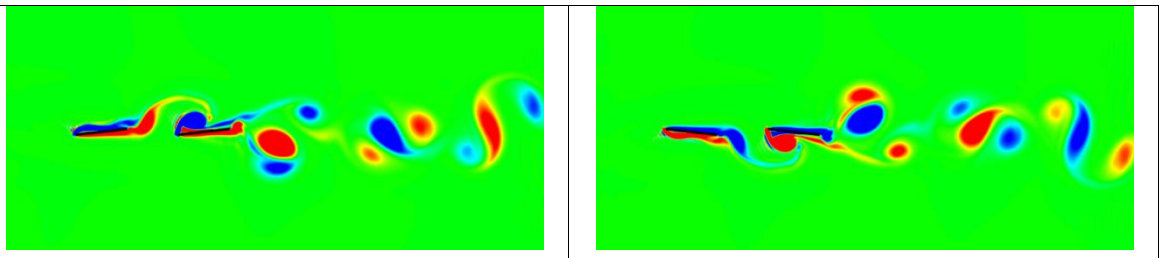

t/T = 0.5 | t/T = 1.0

Fig 9 Vorticity of tandem wings in pitching and plunging

The eigenvalue spectrum of the tandem wing case is shown in figure 10. As usual, the modes are paired by energy level. The distinction in tandem wings is that the energy levels of modes 1 and 2 only accounts for 60% of energy, which is lower compared to that in single wing case (figure 7). The energy levels of mode 3 to 6 are higher. The cumulative energy level of the first 6 modes in tandem wings is similar in the single wing, which is approximately 95%.

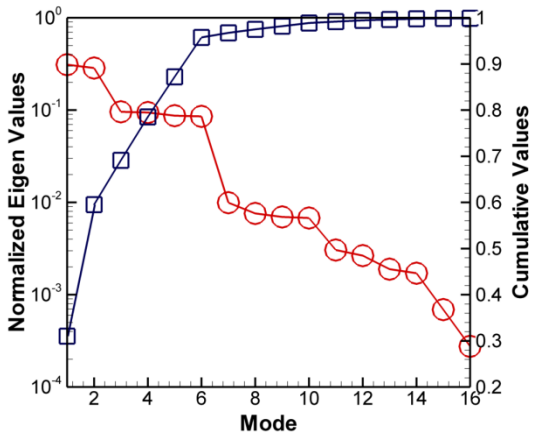

Fig. 10 Eigenvalue spectrum in tandem wings

The velocity modes of tandem wings in pitching and plunging are shown in figure 11. It is interesting to see in higher order modes (3 to 6) that some high energy components exist in the far field. This may indicate the increasingly importance of high order mode in the far field.

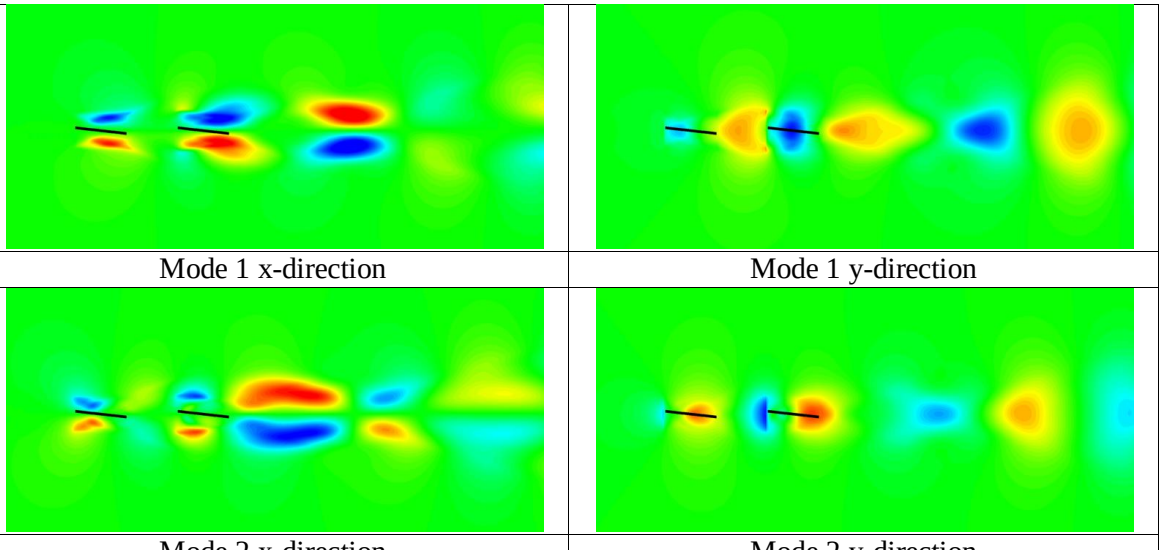

Mode 1 x-direction | Mode 1 y-direction

Mode 2 x-direction | Mode 2 y-direction

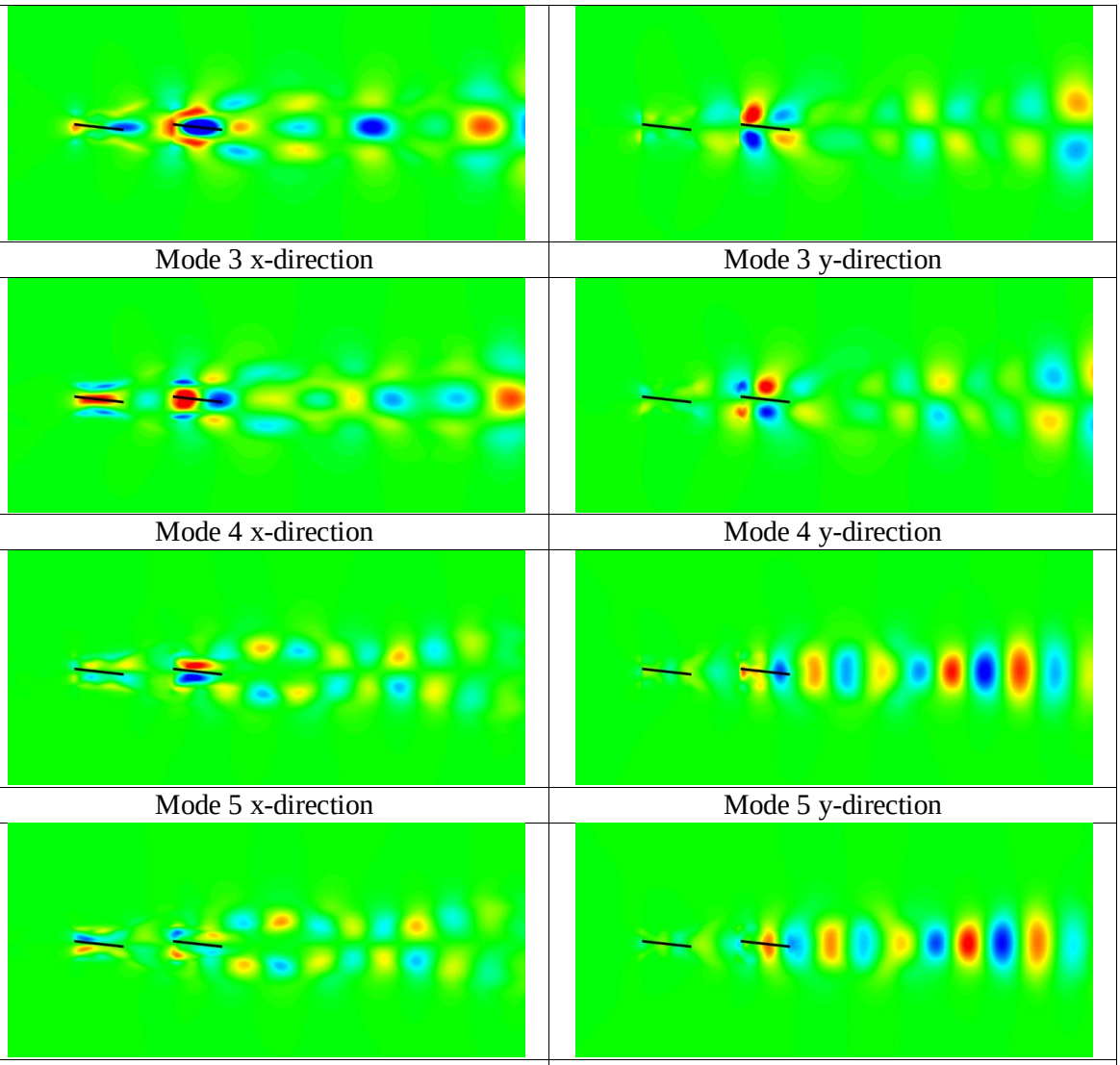

Mode 3 x-direction	Mode 3 y-direction
Mode 4 x-direction	Mode 4 y-direction
Mode 5 x-direction	Mode 5 y-direction
Mode 6 x-direction	Mode 6 y-direction

Figure 11 Velocity mode of tandem wings in pitching and plunging

Acknowledgments

This is work is supported under AFRL Summer Faculty Program (grant#: 667540) and Wright State University Research Challenge grant.

References

1. Dickinson, M.H., F.O. Lehmann, and S.P. Sane, *Wing rotation and the aerodynamic basis of insect flight.* Science, 1999. **284**(5422): p. 1954-1960.
2. Weis-Fogh, T., *Quick Estimates of Flight Fitness in Hovering Animals, Including Novel Mechanisms for Lift Production.* Journal of Experimental Biology, 1973. **59**(1): p. 169-230.

3. Ellington, C.P., et al., *Leading-edge vortices in insect flight.* Nature, 1996. **384**(6610): p. 626-630.
4. Wakeling, J.M., *Dragonfly aerodynamics and unsteady mechanisms: a review.* Odonatologica, 1993. **22**: p. 319.
5. Maybury, W.J. and F.-O. Lehmann, *The fluid dynamics of flight control by kinematic phase lag variation between two robotic insect wings.* Journal of Experimental Biology, 2004. **207**(26): p. 4707-4726.
6. Wang, H., et al., *Measuring wing kinematics, flight trajectory and body attitude during forward flight and turning maneuvers in dragonflies.* Journal of Experimental Biology, 2003. **206**(4): p. 745-757.
7. Ho, S., et al., *Unsteady aerodynamics and flow control for flapping wing flyers.* Progress in Aerospace Sciences, 2003. **39**(8): p. 635-681.
8. Lehmann, *Wing-Wake interaction reduces power consumption in insect tandem wings.* Experiments in Fluids, 2009. **46**(5): p. 765.
9. Sun, M. and S.L. Lan, *A computational study of the aerodynamic forces and power requirements of dragonfly (Aeschna juncea) hovering.* J Exp Biol, 2004. **207**(Pt 11): p. 1887-901.
10. Wang, *Effect of forewing and hindwing interactions on aerodynamic forces and power in hovering dragonfly flight.* Physical Review Letters, 2007. **99**(14): p. 148101.
11. Liang, Z. and H. Dong, *Computational Study of Wing-Wake Interactions between Ipsilateral Wings of Dragonfly in Flight.* AIAA Paper, 2009(2009-4192).
12. Dong, H. and Z. Liang, *Effects of Ipsilateral Wing-Wing Interactions on Aerodynamic Performance of Flapping Wings.* AIAA Paper, (2010-0071).
13. Graham, W.R., J. Peraire, and K.Y. Tang, *Optimal control of vortex shedding using low order models. Part I: Open-loop model development.* International Journal for Numerical Methods in Engineering, 1999. **44**(7): p. 945.
14. Bergmann, M., L. Cordier, and J.-P. Brancher, *Optimal rotary control of the cylinder wake using proper orthogonal decomposition reduced-order model.* Physics of Fluids, 2005. **17**(9): p. 097101-21.
15. Ma, X. and G.E. Karniadakis, *A low-dimensional model for simulating three-dimensional cylinder flow*. 2002, Cambridge Journals Online. p. 181-190.
16. Galletti, B., et al., *Low-order modelling of laminar flow regimes past a confined square cylinder*. 2004, Cambridge Journals Online. p. 161-170.
17. Dipankar, A., T.K. Sengupta, and S.B. Talla, *Suppression of vortex shedding behind a circular cylinder by another control cylinder at low Reynolds numbers*. 2007, Cambridge Journals Online. p. 171-190.
18. Jacob, M.C., et al., *A rod-airfoil experiment as a benchmark for broadband noise modeling.* Theoretical and Computational Fluid Dynamics, 2005. **19**(3): p. 171-196.
19. Smith, T.R., J. Moehlis, and P. Holmes, *Low-Dimensional Modelling of Turbulence Using the Proper Orthogonal Decomposition: A Tutorial.* Nonlinear Dynamics, 2005. **41**(1): p. 275-307.

20. Akhtar, I., A.H. Nayfeh, and C.J. Ribbens, *On the stability and extension of reduced-orderGalerkin models in incompressible flows*. Theor. Comput. Fluid Dyn., 2009. **23**: p. 213–237
21. Akhtar, I., et al., *Hydrodynamics of a biologically inspired tandem flapping foil configuration.* Theoretical and Computational Fluid Dynamics, 2007. **21**(3): p. 155-170.